



Beyond the random phase approximation: Stimulated Brillouin backscatter for finite laser coherence times

Alexander O. Korotkevich,^{1,2} Pavel M. Lushnikov,^{1,2,a)} and Harvey A. Rose^{3,4}

¹Department of Mathematics and Statistics, University of New Mexico, Albuquerque, New Mexico 87131, USA

²Landau Institute for Theoretical Physics, 2 Kosygin Str., Moscow 119334, Russia

³Theoretical Division, Los Alamos National Laboratory, MS-B213, Los Alamos, New Mexico 87545, USA

⁴New Mexico Consortium, Los Alamos, New Mexico 87544, USA

(Received 29 January 2014; accepted 5 January 2015; published online 20 January 2015)

We developed a linear theory of backward stimulated Brillouin scatter (BSBS) of a spatially and temporally random laser beam relevant for laser fusion. Our analysis reveals a new collective regime of BSBS (CBSBS). Its intensity threshold is controlled by diffraction, once cT_c exceeds a laser speckle length, with T_c the laser coherence time. The BSBS spatial gain rate is approximately the sum of that due to CBSBS, and a part which is independent of diffraction and varies linearly with T_c . The CBSBS spatial gain rate may be reduced significantly by the temporal bandwidth of KrF-based laser systems compared to the bandwidth currently available to temporally smoothed glass-based laser systems. © 2015 AIP Publishing LLC. [<http://dx.doi.org/10.1063/1.4906057>]

I. INTRODUCTION

Inertial confinement fusion (ICF) experiments require propagation of intense laser light through underdense plasma. These laser beams are subject to laser-plasma-interaction (LPI) instabilities which can be deleterious to thermonuclear ignition because they lead to loss of target symmetry, loss of target energy and hot electron production.¹ Among LPI, backward stimulated Brillouin scatter (BSBS) has long been considered a serious danger because the damping threshold of BSBS of coherent laser beams is typically several orders of magnitude less than the required laser intensity $\sim 10^{15}$ W/cm² for ICF. BSBS may result in laser energy retracing its path to the laser optical system, possibly damaging laser components.^{1,2} Recent experiments, which for the first time achieved conditions of fusion plasma, demonstrate that large levels of BSBS (up to 10% of reflectivity) are possible.³

The linear theory of LPI instabilities is well developed for coherent laser beams.⁴ However, ICF laser beams are not coherent because temporal and spatial beam smoothing techniques are used to produce laser beams with short enough correlation time, T_c , and lengths to suppress self-focusing.^{1,2,4} Spatial smoothing results in a speckle field of laser intensity fluctuations with transverse correlation length $l_c \simeq F\lambda_0$ and longitudinal correlation length (speckle length) $L_{\text{speckle}} \simeq 7F^2\lambda_0$, where F is the optic f -number and $\lambda_0 = 2\pi/k_0$ is the laser light wavelength (see, e.g., Refs. 5 and 6). There is a long history of LPI instability theory in random laser beams (see, e.g., Refs. 7–9 and references therein). For small enough laser beam correlation time T_c , the spatial gain rate, κ_i , is given by the Random Phase Approximation (RPA). However, beam smoothing for ICF typically has T_c well above the regime of RPA applicability. There are few examples in which the implications of laser beam spatial and temporal incoherence have been analyzed for such T_c . One

exception is forward stimulated Brillouin scattering (FSBS). We have obtained in Refs. 10 and 11 the FSBS dispersion relation for T_c too large for RPA relevance, but still small enough to suppress single laser speckle instabilities.¹² We verified our theory of this “collective” FSBS instability regime with 3D simulations. Similar simulation results had been previously observed.¹³

This naturally leads one to consider the possibility of a collective regime for BSBS (CBSBS). We present 2D and 3D simulation results as evidence for such a regime, and find agreement with a simple theory which finds above the CBSBS threshold that the spatial gain rate for backscatter κ_i , is well approximated by the sum of two contributions. The first contribution is RPA-like, $\kappa_i \propto T_c$, with zero intensity threshold (when light wave damping is neglected). The second contribution has a finite laser intensity threshold. That threshold is within the parameter range of ICF hohlraum plasmas at the National Ignition Facility (NIF)¹ and at the Omega laser facility (OMEGA).¹⁴ This threshold was first predicted in Ref. 15 in the limit $cT_c \gg L_{\text{speckle}}$, where c is the speed of light.^{16,26,27} The second contribution is collective-like because it neglects single speckle contributions and its spatial gain rate is independent of T_c for $cT_c \gg L_{\text{speckle}}$. The CBSBS threshold is applicable for strong and weak acoustic damping coefficient ν_{ia} . The theory accurately predicts κ_i for small $\nu_{ia} \sim 0.01$ which is relevant for gold plasma near the hohlraum wall in NIF and OMEGA experiments.^{1,14} The standard RPA regime is recovered well below the CBSBS threshold for significantly smaller correlation time $cT_c < (4/7\pi)L_{\text{speckle}}$.

The paper is organized as follows. In Sec. II, we introduce the basic equations of BSBS for LPI and the stochastic boundary conditions which model the laser beam’s randomness. In Sec. III, we find the dispersion relations of the linearized BSBS equations. In Sec. IV, their convective and absolute instabilities are analyzed. Section V describes the details of our stochastic simulations of the linearized

^{a)}Electronic address: plushnik@math.unm.edu

equations. In Sec. VI, the conditions of applicability of the dispersion relation are discussed. Section VII considers the estimates for typical ICF experimental conditions. In Sec. VIII the main results of the paper are discussed.

II. BASIC EQUATIONS

Assume that laser beam propagates in plasma with frequency ω_0 along z . The electric field \mathcal{E} is given by

$$\mathcal{E} = (1/2)e^{-i\omega_0 t} [Ee^{ik_0 z} + Be^{-ik_0 z - i\Delta\omega t}] + c.c., \quad (1)$$

where $E(\mathbf{r}, z, t)$ is the envelope of laser beam and $B(\mathbf{r}, z, t)$ is the envelope of backscattered wave, $\mathbf{r} = (x, y)$, and c.c. means complex conjugated terms. Frequency shift $\Delta\omega = -2k_0 c_s$ is determined by coupling of E and B through ion-acoustic wave of phase speed c_s and wavevector $2k_0$ with plasma density fluctuation δn_e given by $\frac{\delta n_e}{n_e} = \frac{1}{2}\sigma e^{2ik_0 z + i\Delta\omega t} + c.c.$, where $\sigma(\mathbf{r}, z, t)$ is the slow envelope (slow provided $\Delta\omega T_c \gg 1$) and n_e is the average electron density, assumed small compared to the critical electron density n_c . We consider a slab model of plasma (plasma parameters are uniform). The coupling of E and B to plasma density fluctuations gives

$$R_{EE}^{-1}E \equiv \left[i(c^{-1}\partial_t + \partial_z) + \frac{1}{2k_0}\nabla^2 \right] E = \frac{k_0 n_e}{4 n_c} \sigma B, \quad (2)$$

$$R_{BB}^{-1}B \equiv \left[i(c^{-1}\partial_t - \partial_z) + \frac{1}{2k_0}\nabla^2 \right] B = \frac{k_0 n_e}{4 n_c} \sigma^* E, \quad (3)$$

$\nabla = (\partial_x, \partial_y)$, and σ is described by the acoustic wave equation coupled to the ponderomotive force $\propto \mathcal{E}^2$ which results in the envelope equation

$$R_{\sigma\sigma}^{-1}\sigma^* \equiv [i(c_s^{-1}\partial_t + 2\nu_{ia}k_0 + \partial_z) - (4k_0)^{-1}\nabla^2]\sigma^* = -2k_0 E^* B. \quad (4)$$

Here, we neglected terms $\propto |E|^2, |B|^2$ in the right-hand side (r.h.s.) which are responsible for self-focusing effects, ν_L is the Landau damping of ion-acoustic wave and $\nu_{ia} = \nu_L/2k_0 c_s$ is the scaled acoustic Landau damping coefficient. E and B are in thermal units (see, e.g., Ref. 10), e.g., $|E|^2 \equiv I = (1/4)(v_{osc}/v_e)^2$, with v_{osc} the quiver velocity of the electron in the laser's electromagnetic field and v_e is the electron thermal speed.

We use a simple model of induced spatial incoherence beam smoothing¹⁷ which defines stochastic boundary conditions at $z=0$ for the spatial Fourier transform (over \mathbf{r}) of $E, \hat{E}(\mathbf{k})$ ¹⁰

$$\hat{E}(\mathbf{k}, z=0, t) = |E_{\mathbf{k}}| \exp[i\phi_{\mathbf{k}}(t)], \\ \langle \exp(i[\phi_{\mathbf{k}}(t) - \phi_{\mathbf{k}'}(t')]) \rangle = \delta_{\mathbf{k}\mathbf{k}'} \exp(-|t-t'|/T_c), \quad (5)$$

where

$$|E_{\mathbf{k}}| = \text{const}, k < k_m; \quad E_{\mathbf{k}} = 0, k > k_m, \quad (6)$$

is chosen as the idealized ‘‘top hat’’ model of NIF optics.¹⁸ Here $\langle \dots \rangle$ means the averaging over the ensemble of stochastic realizations of boundary conditions, $k_m \simeq k_0/(2F)$ is the

top hat width and the average intensity, $\langle I \rangle \equiv \langle |E|^2 \rangle = I$ determines the constant.

III. LINEARIZED EQUATIONS AND DISPERSION RELATIONS

In linear approximation, assuming $|B| \ll |E|$ so that only the laser beam is BSBS unstable, we neglect the right hand side (r.h.s.) of Eq. (2). The resulting linear equation with boundary condition (5) may be solved exactly in Fourier space

$$E(\mathbf{r}, z, t) = \sum_j E_{\mathbf{k}_j}, \quad (7) \\ E_{\mathbf{k}_j} = |E_{\mathbf{k}_j}| \exp[i(\phi_{\mathbf{k}_j}(t - z/c) + \mathbf{k}_j \cdot \mathbf{r} - \mathbf{k}_j^2 z/2k_0)],$$

where we take sum over the transverse Fourier harmonics \mathbf{k}_j .

Figure 1 shows the spatial gain rate, κ_i , defined by the growth of backscattered light intensity $\langle |B|^2 \rangle \propto e^{-2\kappa_i z}$ ($\langle |B|^2 \rangle \propto e^{-2\kappa_i z}$) as a function of the re-scaled correlation time \tilde{T}_c obtained from our numerical solution of the stochastic linear

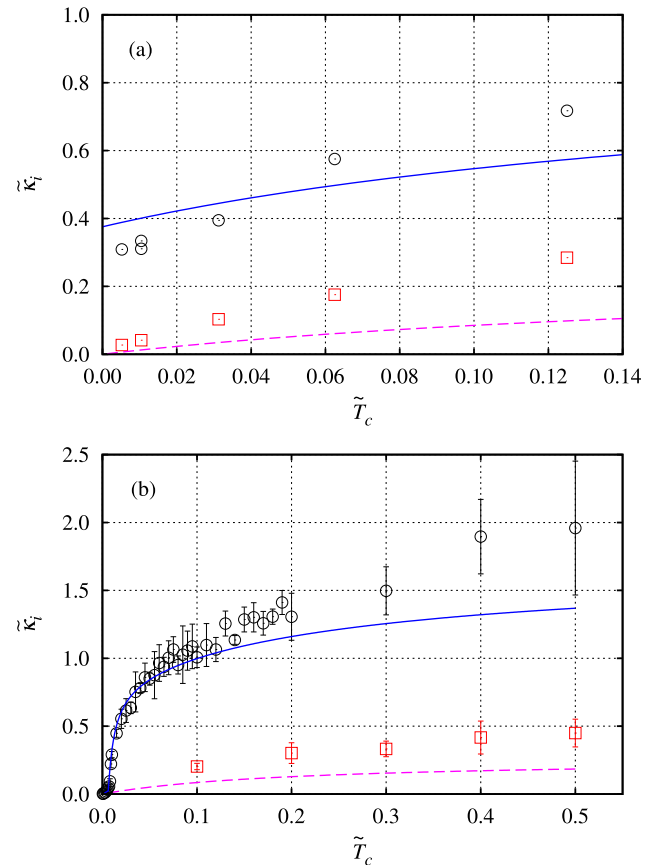


FIG. 1. Dimensionless spatial gain rate $\tilde{\kappa}_i \equiv \kappa_i 4F^2/k_0$ of BSBS obtained from stochastic simulations of (3)–(7) compared with the sum of spatial gain rates $\tilde{\kappa}_B + \tilde{\kappa}_\sigma$ (obtained by solving (17) and (37)). The scaled damping rate $\mu = 5.12$ is used (e.g., it corresponds to $\nu_{ia} = 0.01, F = 8$). (a) 3D simulations with $c_s/c = 0, \tilde{I} = 2$ (circles) and $\tilde{I} = 1$ (squares). The scaled dimensionless laser intensity \tilde{I}, μ , and the scaled correlation time \tilde{T}_c are defined in (8). Solid and dashed lines show $\tilde{\kappa}_B + \tilde{\kappa}_\sigma$ for $\tilde{I} = 2$ and $\tilde{I} = 1$, respectively. If $\tilde{\kappa}_\sigma < 0$ then $\tilde{\kappa}_B + \tilde{\kappa}_\sigma$ is replaced by $\tilde{\kappa}_B$. (b) 2D simulations with $c/c_s = 500, \tilde{I} = 3$ (circles) and $\tilde{I} = 1$ (squares). Error bars are also shown. Solid and dashed lines show $\tilde{\kappa}_B + \tilde{\kappa}_\sigma$ for $\tilde{I} = 3$ and $\tilde{I} = 1$, respectively, for both (a) and (b). The details of simulation method are provided in Sec. V.

equations (3)–(7) (details of numerical simulations are provided in Sec. V). The re-scaled damping rate, μ , the re-scaled laser intensity, \tilde{I} , and the re-scaled coherence time, \tilde{T}_c

$$\tilde{T}_c \equiv \frac{T_c}{T_s}, \quad \mu \equiv 2\nu_{ia}k_0^2/k_m^2, \quad \tilde{I} \equiv \frac{4F^2 n_e I}{\nu_{ia} n_c}, \quad (8)$$

prove useful. \tilde{T}_c is the correlation time T_c in units of the acoustic transit time along the speckle length

$$T_s = \frac{4F^2}{k_0 c_s}. \quad (9)$$

Note that definition of \tilde{T}_c is different by a factor $1/2F$ from the definition used for FSBS,^{10,11} where units of the transverse acoustic transit time through speckle were used. We use dimensionless units with $k_0/k_m^2 = 4F^2/k_0$ as the z -direction unit of length, $1/k_m = 2F/k_0$ as the transverse unit of length and T_s is the time unit. $\langle \dots \rangle$ means averaging over the statistics of laser beam fluctuations (5). μ is the damping rate in units of $1/T_s$. (See also Figure 11 below for illustration of intensity normalization in comparison with physical units.)

We now relate κ_i to the spatial gain rates for $\langle B \rangle$ and $\langle \sigma^* \rangle$ (we designate them κ_B and κ_σ , respectively). In general, gain rates of mean amplitudes give a lower bound to κ_i . Note, according to Figure 2, σ is almost coherent on a time scale T_c . We also see from Figure 2 that B simply inherits the coherence time T_c imposed at the boundary for E . *A priori*, one expects that density fluctuations σ which propagate as ion acoustic waves, Eq. (4) without the E^*B source, do not respond efficiently to arbitrarily rapid variations in time of the source because of ion inertia. This expectation is borne out by results which show a longer correlation time of σ (in comparison with T_c) as seen in Figure 2.

First, we develop a suitable approximation for κ_σ . Solve Eq. (3) for B , insert that expression for B into (4) and ensemble average to obtain

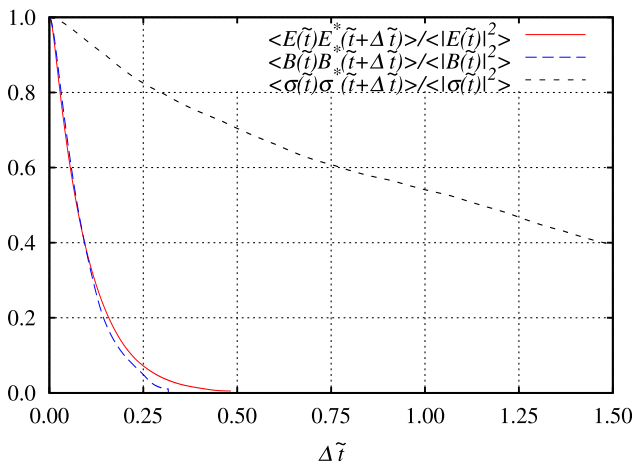


FIG. 2. Normalized autocorrelation functions vs. a dimensionless time shift $\Delta\tilde{t}$ for E , B , and σ : $\langle E(\vec{r}, \vec{z}, \tilde{t})E^*(\vec{r}, \vec{z}, \tilde{t} + \Delta\tilde{t}) \rangle / \langle |E(\tilde{t})|^2 \rangle$, $\langle B(\vec{r}, \vec{z}, \tilde{t})B^*(\vec{r}, \vec{z}, \tilde{t} + \Delta\tilde{t}) \rangle / \langle |B(\tilde{t})|^2 \rangle$, and $\langle \sigma(\vec{r}, \vec{z}, \tilde{t})\sigma^*(\vec{r}, \vec{z}, \tilde{t} + \Delta\tilde{t}) \rangle / \langle |\sigma(\tilde{t})|^2 \rangle$ with $\tilde{I} = 3$, $\tilde{T}_c = 0.1$, and $\mu = 5.12$ from stochastic simulations of (3)–(7). It is seen that B is correlated at the same time \tilde{T}_c as E while σ is correlated at much larger times. These autocorrelation functions are independent of \vec{r} and \vec{z} as detailed in Sec. V.

$$R_{\sigma\sigma}^{-1}\langle \sigma^* \rangle = -(k_0^2/2)(n_e/n_c)\langle E^*R_{BB}\sigma^*E \rangle. \quad (10)$$

We recover the Bourret approximation^{8,9} by approximating the r.h.s. of Eq. (10) as $\langle E^*R_{BB}\sigma^*E \rangle \simeq \langle E^*R_{BB}E \rangle \langle \sigma^* \rangle$. Then Eq. (10) is reduced to a closed expression for $\langle \sigma^* \rangle$ as

$$R_{\sigma\sigma}^{-1}\langle \sigma^* \rangle = -(k_0^2/2)(n_e/n_c)\langle E^*R_{BB}E \rangle \langle \sigma^* \rangle. \quad (11)$$

The Fourier transform over \mathbf{r} of the response function R_{BB} is given by the explicit expression

$$\hat{R}_{BB}(\mathbf{k}, z, t) = -ic\delta(z + ct)\exp\left[i\frac{k^2}{2k_0}z\right]\Theta(-z), \quad (12)$$

where $\Theta(z)$ is the Heaviside step function. In \mathbf{r} , z space we obtain

$$\begin{aligned} R_{\sigma\sigma}^{-1}\langle \sigma^*(\mathbf{r}, z, t) \rangle &= -(k_0^2/2)(n_e/n_c) \iiint d\mathbf{r}' dz' dt' \\ &\times R_{BB}(\mathbf{r} - \mathbf{r}', z - z', t - t') \\ &\times C^*(\mathbf{r} - \mathbf{r}', z - z', t - t') \\ &\times \langle \sigma^*(\mathbf{r}', z', t') \rangle, \end{aligned} \quad (13)$$

where the kernel $R_{BB}(\mathbf{r}, z, t)$ of the response function R_{BB} is the inverse Fourier transform of (12). Here, the laser beam correlation function C is defined using Eq. (7) as

$$\begin{aligned} C(\mathbf{r} - \mathbf{r}', z - z', t - t') &\equiv \langle E(\mathbf{r}, z, t)E^*(\mathbf{r}', z', t') \rangle \\ &= \sum_j |E_{\mathbf{k}_j}|^2 \exp\left[i\mathbf{k}_j \cdot (\mathbf{r} - \mathbf{r}') - i\frac{\mathbf{k}_j^2}{2k_0}(z - z')\right. \\ &\quad \left. - |t - t' - (z - z')/c|/T_c\right]. \end{aligned} \quad (14)$$

The particular form of C for the top hat model is defined by Eqs. (5) and (6).

If one looks for solutions of Eq. (13) in exponential form $\langle \sigma^* \rangle \propto e^{i(\kappa z + \mathbf{k} \cdot \mathbf{r} - \omega t)}$, then the exponential time dependence of Eq. (14) allows explicit evaluation of all integrals in Eqs. (12) and (13) to arrive at the following dispersion relation in dimensionless units:

$$\begin{aligned} -i\tilde{\omega} + \mu + i\tilde{\kappa} - (i/4)\tilde{k}^2 \\ = 8iF^4 \frac{n_e}{n_c} \sum_{j=1}^N \frac{|E_{\mathbf{k}_j}|^2}{\tilde{\omega} \frac{c_s}{c} + \tilde{\kappa} - \tilde{k}_j^2 - \frac{\tilde{k}^2}{2} - \tilde{\mathbf{k}}_j \cdot \tilde{\mathbf{k}} + 2i \frac{c_s}{c} \frac{1}{\tilde{T}_c}}, \end{aligned} \quad (15)$$

where $\tilde{\omega} \equiv \omega 4F^2 / (k_0 c_s)$, $\tilde{\kappa} \equiv \kappa 4F^2 / k_0$, the vectors $\tilde{\mathbf{k}}_j \equiv \mathbf{k}_j 2F / k_0$ span the top hat, Eqs. (5) and (6), and $I = \sum_j |E_{\mathbf{k}_j}|^2$. In dimensional units, Eq. (15) takes the equivalent form

$$\begin{aligned} -i\omega + 2\nu_{ia}k_0 c_s + i\kappa c_s - \frac{i}{4k_0}k^2 c_s \\ = \frac{ik_0^3 c_s n_e}{2n_c} \times \sum_{j=1}^N \frac{|E_{\mathbf{k}_j}|^2}{\omega \frac{k_0}{c} + k_0 \kappa - k_j^2 - \frac{k^2}{2} - \mathbf{k}_j \cdot \mathbf{k} + 2i \frac{k_0}{c} \frac{1}{T_c}}. \end{aligned} \quad (16)$$

For the top hat model in the continuous limit $N \rightarrow \infty$, the sum in Eq. (15) is replaced by an integral, giving for the most unstable mode $\mathbf{k} = 0$

$$\Delta_\sigma(\tilde{\omega}, \tilde{\kappa}) = -i\tilde{\omega} + \mu + i\tilde{\kappa} + i\frac{\mu}{4}\tilde{I}\ln\frac{1 - \tilde{\kappa} - \tilde{\omega}\frac{c_s}{c} - 2i\frac{c_s}{c}\frac{1}{\tilde{T}_c}}{-\tilde{\kappa} - \tilde{\omega}\frac{c_s}{c} - 2i\frac{c_s}{c}\frac{1}{\tilde{T}_c}} = 0. \quad (17)$$

In dimensional units Eq. (17) takes the following form:

$$-i\omega + 2\nu_{ia}k_0c_s + i\kappa c_s + 2ik_0c_sF^2\frac{n_e}{n_c}\ln\frac{\frac{k_0}{4F^2} - \kappa - \frac{\omega}{c} - 2i\frac{1}{cT_c}}{-\kappa - \frac{\omega}{c} - 2i\frac{1}{cT_c}} = 0. \quad (18)$$

The dispersion relation Eq. (17) has a branch cut in the complex κ -plane connecting two branch points $\tilde{\kappa}_1 = 1 - \tilde{\omega}\frac{c_s}{c} - 2i\frac{c_s}{c}\frac{1}{\tilde{T}_c}$ and $\tilde{\kappa}_2 = -\tilde{\omega}\frac{c_s}{c} - 2i\frac{c_s}{c}\frac{1}{\tilde{T}_c}$. In the discrete case, Eq. (15) with $N \gg 1$, instead of a branch cut this discrete dispersion relation has solutions located near the line connecting $\tilde{\kappa}_1$ and $\tilde{\kappa}_2$ in the complex $\tilde{\kappa}$ -plane. These solutions of the discrete case are highly localized around some \mathbf{k}_j so they cannot be approximated by Eq. (17) but they are stable for $N \gg 1$ and can be ignored as we take the limit $N \rightarrow \infty$. Other solutions of the discrete case in that limit converge to the solution of Eq. (17). Thus it is sufficient to consider Eq. (17) only.

We analyze the convective instability in Eq. (17) by maximizing the convective instability spatial gain rate $\tilde{\kappa}_\sigma \equiv \text{Im}(\tilde{\kappa})$ over real values of $\tilde{\omega}$. Solving real and imaginary part of Eq. (17) gives $\tilde{\kappa}(\tilde{\omega})$. However, Eq. (17) is transcendental, preventing explicit determination of $\tilde{\kappa}(\tilde{\omega})$. Instead, we differentiate Eq. (17) over $\tilde{\omega}$ assuming that $\tilde{\kappa}(\tilde{\omega})$ solves Eq. (17). It gives

$$\frac{\Delta_\sigma(\tilde{\omega}, \tilde{\kappa}(\tilde{\omega}))}{d\tilde{\omega}} = \left[\frac{\partial\Delta_\sigma(\tilde{\omega}, \tilde{\kappa})}{\partial\tilde{\omega}} + \tilde{\kappa}'(\tilde{\omega})\frac{\partial\Delta_\sigma(\tilde{\omega}, \tilde{\kappa})}{\partial\tilde{\kappa}} \right] \Big|_{\kappa=\kappa(\tilde{\omega})} = 0, \quad (19)$$

where $\tilde{\kappa}'(\tilde{\omega}) \equiv \frac{d\tilde{\kappa}(\tilde{\omega})}{d\tilde{\omega}}$. The maximum of $\tilde{\kappa}_\sigma = \text{Im}(\tilde{\kappa})$ over $\tilde{\omega}$ requires

$$\text{Im}[\kappa'(\tilde{\omega})] = 0, \quad (20)$$

while $\text{Re}[\kappa'(\tilde{\omega})]$ has to be determined. Using the conditions that the real part of (19) is zero, subject to the constraint of Eq. (20), one obtains for general $\text{Im}(\tilde{\omega})$ that either

$$\text{Re}[\kappa'(\tilde{\omega})] = -\frac{c_s}{c}, \quad (21)$$

or

$$\tilde{\omega} = \frac{1 - 2\text{Re}(\tilde{\kappa})}{2\frac{c_s}{c}}. \quad (22)$$

However, when Eq. (21) is plugged into the imaginary part of Eq. (19), one obtains $c_s/c = -1$ which is unphysical.

Instead, when Eq. (22) is plugged into the imaginary part of Eq. (19), one obtains a physical solution. We plug in Eq. (22) into the dispersion relation, Eq. (17), and then the logarithm of (17) turns into

$$i\frac{\mu}{4}\tilde{I}\ln\frac{\frac{i}{2} + \text{Im}(\tilde{\kappa}) + 2\frac{c_s}{c}\frac{1}{\tilde{T}_c}}{-\frac{i}{2} + \text{Im}(\tilde{\kappa}) + 2\frac{c_s}{c}\frac{1}{\tilde{T}_c}},$$

which is purely real valued. Then the imaginary part of Eq. (17) is no longer transcendental. Solving it for $\text{Re}(\tilde{\kappa})$ with the use of (22), one obtains an exact expression for the value of ω which maximizes $\tilde{\kappa}_\sigma = \text{Im}(\tilde{\kappa})$. It is achieved at

$$\tilde{\omega} = \text{Re}(\tilde{\kappa}) = \frac{1}{2\left(1 + \frac{c_s}{c}\right)}. \quad (23)$$

The threshold of the convective instability $\tilde{I} = \tilde{I}_{convthresh}$ corresponds to $\tilde{\kappa}_\sigma = \text{Im}(\tilde{\kappa}) = 0$. Evaluating the real part of Eq. (17) at that threshold together with Eq. (23) implies that the convective CBSBS threshold is given by

$$\tilde{I}_{convthresh} = \frac{2}{\arctan\left(\frac{c\tilde{T}_c}{4c_s}\right)}. \quad (24)$$

In non-scaled units equation (24) takes the following form:

$$I_{convthresh} = \frac{\nu_{ia}n_c}{4F^2n_e} \frac{2}{\arctan\left(\frac{k_0cT_c}{16F^2}\right)}. \quad (25)$$

Above threshold, $\tilde{I} > \tilde{I}_{convthresh}$, the spatial gain rate is positive, $\tilde{\kappa}_\sigma > 0$. Assuming that

$$\frac{c\tilde{T}_c}{4c_s} \gg 1, \quad (26)$$

we obtain from (24) that

$$\tilde{I}_{convthresh} = \frac{4}{\pi} \left(1 + \frac{8c_s}{\pi c\tilde{T}_c}\right) + O\left(\frac{4c_s}{c\tilde{T}_c}\right)^2 \simeq \frac{4}{\pi}. \quad (27)$$

Condition (26) means that during a laser coherence time, T_c , light travels far further than a speckle length, $L_{speckle} \ll cT_c$. We conclude from Eqs. (26) and (27), that the convective threshold, (24), is an insensitive function of the laser coherence time in that limit.

In non-scaled units Eq. (27) reduces to

$$I_{convthresh} = \frac{\nu_{ia}n_c}{4F^2n_e} \frac{2}{\arctan\left(\frac{k_0cT_c}{16F^2}\right)} \simeq \frac{\nu_{ia}n_c}{4F^2n_e} \frac{4}{\pi}, \quad (28)$$

where the intensity is in thermal units.

Above the convective threshold, $\tilde{I} > \tilde{I}_{convthresh}$, there are two solutions of Eq. (17). One of these solutions does not

cross the real κ axis from below as the complex contour $Im(\omega) \rightarrow 0$. Thus the standard analysis of convective vs. absolute instabilities (see, e.g., Ref. 19) implies that this solution does not describe instability. Assuming $\frac{c\tilde{T}_c}{4c_s} \gg 1$ and $\mu \gg 1$ that stable solution is given by

$$\tilde{\kappa}_\sigma = (1/2)[\mu + (\mu^2 - \tilde{I}\mu)^{1/2}], \quad (29)$$

coinciding with the stable branch in the coherent case (see, e.g., Ref. 4). The second solution does cross the real κ axis so it is convectively unstable and we consider only that solution below.

In the limit $\frac{c\tilde{T}_c}{4c_s} \gg 1$ and assuming that \tilde{I} is just above the convective threshold, Eq. (24), we obtain from Eqs. (17), (23), and (24) that

$$\tilde{\kappa}_\sigma = \mu \left(\frac{\pi}{4} - 2 \frac{c_s}{c\tilde{T}_c} \right) \frac{\tilde{I} - \tilde{I}_{convthresh}}{\mu \tilde{I}_{convthresh} - 1}. \quad (30)$$

This expression is valid for $\mu > \tilde{I}_{convthresh}^{-1} \simeq \frac{\pi}{4}$, while for $\mu \leq \tilde{I}_{convthresh}^{-1}$ the convective threshold coincides with the absolute instability threshold.

In the limit $c/c_s \rightarrow \infty$ for any fixed \tilde{T}_c , the spatial gain rate $\tilde{\kappa}_\sigma$ is independent of \tilde{T}_c and is given by the corresponding solution of the transcendental equation $2(\tilde{\kappa}_\sigma - \mu) + \mu \tilde{I} \arctan(1/2\tilde{\kappa}_\sigma) = 0$. We refer to $\tilde{\kappa}_\sigma$ as the collective-like branch of instability because it is independent on \tilde{T}_c . For finite but small $c_s/c \ll 1$ and $\tilde{I} > \tilde{I}_{convthresh}$, there is sharp transition of $\tilde{\kappa}_\sigma$ as a function of \tilde{T}_c , from 0 for $\tilde{T}_c = 0$ to \tilde{T}_c -independent value of $\tilde{\kappa}_\sigma$ as seen in Figure 3.

The spatial gain rate of backscattered light amplitude, κ_B , is obtained in a similar way. Statistical averaging of Eq. (3) for $\langle B \rangle$ gives

$$R_{BB}^{-1}\langle B \rangle = -(k_0^2/2)(n_e/n_c)\langle ER_{\sigma\sigma}E^*B \rangle. \quad (31)$$

We again recover the Bourret approximation^{8,9} by approximating the r.h.s. of Eq. (31) as $\langle ER_{\sigma\sigma}E^*B \rangle \simeq \langle ER_{\sigma\sigma}E^* \rangle \langle B \rangle$. Then Eq. (31) is reduced to a closed expression for $\langle B \rangle$ as follows:

$$R_{BB}^{-1}\langle B \rangle = -(k_0^2/2)(n_e/n_c)\langle ER_{\sigma\sigma}E^* \rangle \langle B \rangle. \quad (32)$$

The Fourier transform over \mathbf{r} of the response function $R_{\sigma\sigma}$ is given by the explicit expression

$$\hat{R}_{\sigma\sigma}(\mathbf{k}, z, t) = -ic_s \delta(z - c_s t) \exp \left[\left(i \frac{k^2}{4k_0} - 2\nu_{id} k_0 \right) z \right] \Theta(z). \quad (33)$$

The inverse Fourier transform of Eq. (33) results in the integral form of $R_{\sigma\sigma}$. Writing that integral in the r.h.s. of Eq. (32) explicitly we obtain

$$R_{BB}^{-1}\langle B(\mathbf{r}, z, t) \rangle = -(k_0^2/2)(n_e/n_c) \iiint d\mathbf{r}' dz' dt' \times R_{\sigma\sigma}(\mathbf{r} - \mathbf{r}', z - z', t - t') C^* \times (\mathbf{r} - \mathbf{r}', z - z', t - t') \times \langle B(\mathbf{r}', z', t') \rangle, \quad (34)$$

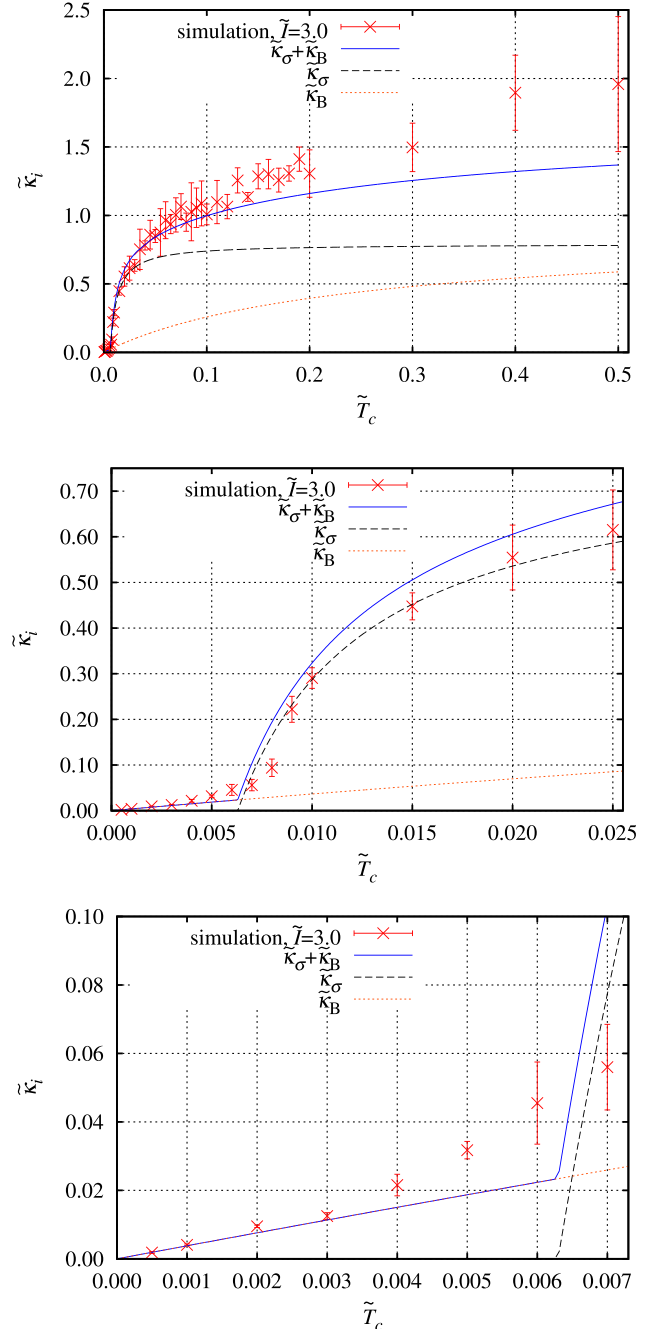


FIG. 3. BSBS spatial gain rates $\tilde{\kappa}_B + \tilde{\kappa}_\sigma$, $\tilde{\kappa}_B$ and $\tilde{\kappa}_\sigma$ compared with the spatial gain rate $\tilde{\kappa}_i$ obtained from same stochastic simulations as in Figure 1(b) (with $\tilde{I} = 3$ and $\mu = 5.12$). (a) Full range of \tilde{T}_c is shown. (b) Intermediate zoom into smaller value of \tilde{T}_c . It is seen that as \tilde{T}_c decreases below $\simeq 0.008$, $\tilde{\kappa}_i$ starts to deviate from $\tilde{\kappa}_B + \tilde{\kappa}_\sigma$. It is seen that $\tilde{\kappa}_\sigma$ vanishes at the convective threshold (24), which corresponds to $\tilde{T}_c = \frac{4c_s}{c} \tan(2/\tilde{I}) = 0.00629\dots$ (c) Zoom into the smallest values of \tilde{T}_c . It is seen that for $\tilde{T}_c \lesssim 0.003$, $\tilde{\kappa}_i$ converges to the RPA result (39) (given by $\tilde{\kappa}_B$ in that limit).

where the kernel $R_{\sigma\sigma}(\mathbf{r}, z, t)$ of the response function $R_{\sigma\sigma}(\mathbf{x}, z, t)$ is the inverse Fourier transform of Eq. (33) and C is given by Eq. (14).

We look for solution of Eq. (13) in exponential form $\langle B \rangle \propto e^{i(kz + \mathbf{k}\cdot\mathbf{r} - \omega t)}$, and then the exponential time dependence of C allows one to evaluate all integrations in Eqs. (33) and (34) explicitly to arrive at the following dispersion relation in dimensionless units:

$$i\tilde{\omega} \frac{c_s}{c} + i\tilde{\kappa} - (i/2)\tilde{\kappa}^2 = 8iF^4 \frac{n_e}{n_c} \times \sum_{j=1}^N \frac{|E_{\mathbf{k}_j}|^2}{-\tilde{\omega} + \tilde{\kappa} + \frac{\tilde{\kappa}_j^2}{4} - \frac{\tilde{\kappa}^2}{4} + \frac{\tilde{\mathbf{k}}_j \cdot \tilde{\mathbf{k}}}{2} - i\mu - i\left(1 - \frac{c_s}{c}\right) \frac{1}{\tilde{T}_c}}. \quad (35)$$

In dimensional units, Eq. (35) takes the equivalent form

$$i\omega \frac{1}{c} + i\kappa - \frac{i}{2k_0} k^2 = \frac{ik_0^3 n_e}{2n_c} \sum_{j=1}^N \frac{|E_{\mathbf{k}_j}|^2}{-\omega \frac{k_0}{c_s} + k_0 \kappa + \frac{k_j^2}{4} - \frac{k^2}{4} + \frac{\mathbf{k}_j \cdot \mathbf{k}}{2} - i2\nu_{ia} k_0^3 c_s - i \frac{k_0}{c_s T_c} \left(1 - \frac{c_s}{c}\right)}. \quad (36)$$

For the top hat model in the continuous limit $N \rightarrow \infty$, the sum in Eq. (35) is replaced by an integral. As in Eq. (15), we consider only the most unstable mode $\mathbf{k}=0$. Also we note that the diffraction term $k_j^2/4 < 1/4$ in the denominator of Eq. (35) is small compared with the terms $\mu + (1 - \frac{c_s}{c}) \frac{1}{\tilde{T}_c} \gg 1$. Neglecting that diffraction contribution and using the condition $c_s/c \ll 1$ we obtain from Eq. (35) the dispersion relation

$$\Delta_B(\tilde{\omega}, \tilde{\kappa}) = -\tilde{\kappa} + \frac{\mu \tilde{T}_c}{4} \frac{1}{\tilde{\kappa} - \tilde{\omega} - i\mu - i \frac{1}{\tilde{T}_c}} = 0. \quad (37)$$

We analyze the convective instability in Eq. (37) by maximizing the convective instability spatial gain rate $\tilde{\kappa}_B \equiv \text{Im}(\tilde{\kappa})$ over real values of $\tilde{\omega}$. Eq. (37) does not have a convective threshold (provided we neglect light wave damping). The maximum of $\tilde{\kappa}_B$ in Eq. (37) is achieved at $\tilde{\omega} = \text{Re}(\tilde{\kappa}) = 0$ and one then obtains

$$\tilde{\kappa}_B = \frac{1 + \mu \tilde{T}_c}{2\tilde{T}_c} - \frac{\left[(1 + \mu \tilde{T}_c)^2 - \mu \tilde{T}_c^2\right]^{1/2}}{2\tilde{T}_c}. \quad (38)$$

For $\tilde{T}_c < \mu^{-1}$ and $\tilde{T}_c \lesssim 1$, we obtain from Eq. (38) that $\tilde{\kappa}_B$ has near-linear dependence on \tilde{T}_c

$$\tilde{\kappa}_B \simeq \frac{\mu \tilde{T}_c}{4}, \quad (39)$$

which is typical for RPA results. It suggests that we refer $\tilde{\kappa}_B$ as the RPA-like branch of instability.

In dimensional units Eqs. (37) and (39) take the following form:

$$\kappa + k_0^2 \frac{n_e}{2n_c} I \frac{1}{\kappa - \frac{\omega}{c_s} - 2ik_0\nu_{ia} - i \frac{1}{c_s T_c}} = 0, \quad (40)$$

$$\kappa_B \simeq k_0^2 c_s \nu_{ia} \frac{n_e I T_c}{n_c 2}.$$

One may solve Eqs. (17) and (37) numerically for $\tilde{\kappa}_\sigma$ and $\tilde{\kappa}_B$, respectively, for given $\tilde{\omega}$. We choose $\tilde{\omega} = 0.5$ in (17) and (37) to maximize $\tilde{\kappa}_\sigma$. Note that choosing instead $\tilde{\kappa}_B$ at $\tilde{\omega} = 0$ (to maximize $\tilde{\kappa}_B$) would give only a small shift in $\tilde{\kappa}_B$ and lead to indistinguishable changes in all the figures. Figures 1(a) and 1(b) show that the expression $\tilde{\kappa}_B + \tilde{\kappa}_\sigma$ is a

reasonably good approximation to $\tilde{\kappa}_i$ above the convective threshold (24) for $\tilde{T}_c \leq 0.1$ which is the main result of this paper. Below this threshold analytical and numerical results are only in qualitative agreement. We replace $\tilde{\kappa}_B + \tilde{\kappa}_\sigma$ by $\tilde{\kappa}_B$ in that case because for very small \tilde{T}_c the value of $\tilde{\kappa}_B$ converges to $\tilde{\kappa}_i$ as shown in Figure 3(c).

Figure 3 compares the spatial gain rate $\tilde{\kappa}_B + \tilde{\kappa}_\sigma$, $\tilde{\kappa}_B$ and $\tilde{\kappa}_\sigma$ with the spatial gain rate $\tilde{\kappa}_i$ obtained from same stochastic simulations as in Figure 1(b) (with $\tilde{I} = 3$). It is seen that $\tilde{\kappa}_B + \tilde{\kappa}_\sigma$ is in very good agreement with $\tilde{\kappa}_i$ for $\tilde{T}_c \leq 0.1$ while $\max(\tilde{\kappa}_B, \tilde{\kappa}_\sigma)$ is not. We conclude that the simple choice of the most unstable branch between $\tilde{\kappa}_B$ and $\tilde{\kappa}_\sigma$,⁹ i.e., choosing $\max(\tilde{\kappa}_B, \tilde{\kappa}_\sigma)$, does not provide agreement with simulations. We also recall that $\tilde{\kappa}_B$ and $\tilde{\kappa}_\sigma$ are calculated based on the average of amplitudes $\langle B \rangle$ and $\langle \sigma^* \rangle$, while we determine $\tilde{\kappa}_i$ from $\langle |B|^2 \rangle$. It implies that $\tilde{\kappa}_i \geq \max(\tilde{\kappa}_B, \tilde{\kappa}_\sigma)$ in agreement with Figure 3. In Sec. VI, we discuss the applicability of the dispersion relations (17) and (37) and recover the limit of small \tilde{T}_c in which $\max(\tilde{\kappa}_B, \tilde{\kappa}_\sigma)$ converges to $\tilde{\kappa}_i$.

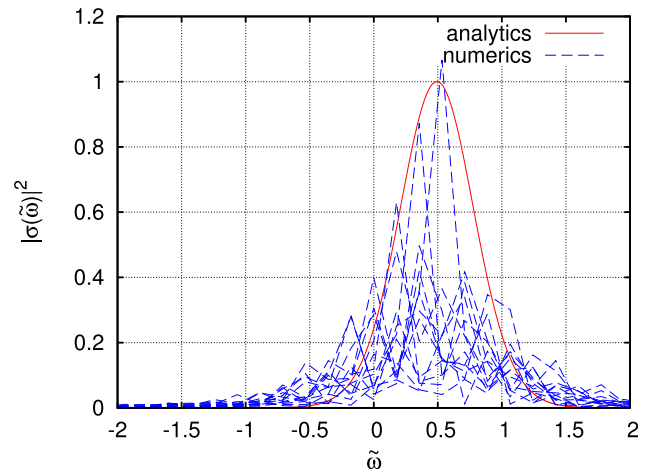


FIG. 4. Dashed lines show a power spectrum $|\sigma(\mathbf{k}, z, t)|^2$ as a function of ω obtained from simulations with amplification length (we measure the spectrum at this distance $L_{\text{amplification}}$ from the left boundary of the system in order to avoid influence of transition layers discussed in Section V) $L_{\text{amplification}} = 50$, $\tilde{I} = 3$, $\mu = 5.12$, and $\tilde{T}_c = 0.1$. Different dashed curves correspond to different Fourier modes in \mathbf{k} located near the center of top-hat, $-0.2 \leq \tilde{k} \leq 0.2$. The highest peak corresponds to $\mathbf{k} = 0$. Solid line shows $\exp(2L_{\text{amplification}} [\tilde{\kappa}_B(\omega) + \tilde{\kappa}_\sigma(\omega)])$. All curves are normalized by $\exp(2L_{\text{amplification}} [\tilde{\kappa}_B(\omega = 0) + \tilde{\kappa}_\sigma(\omega = 0)])$. Roughness of curves is due to the finite simulation time, $\tilde{t}_{\text{tot}} = 35$. Fourier modes are peaked around $\omega = 0.5$.

Figure 4 shows that the Fourier modes of $\sigma(\mathbf{k}, z, t)$ in simulations are indeed peaked around $\omega = 0.5$. It confirms that our choice $\omega = 0.5$ for the analytical theory is optimal.

The qualitative explanation why $\kappa_B + \kappa_\sigma$ is a good approximation to κ_i is based on the following argument. First imagine that B propagates linearly and not coupled to the fluctuations of σ^* , so its source is $\sigma^*E \rightarrow \langle \sigma^* \rangle E$ in r.h.s. of Eq. (3). If $\langle \sigma^* \rangle \propto e^{\kappa_\sigma z}$ grows slowly with z (i.e., if $\langle \sigma^* \rangle$ changes a little over the speckle length L_{speckle} and time T_c), then so will $\langle |B|^2 \rangle$ at the rate $2\kappa_\sigma$. But if the total linear response R_{BB}^{tot} (R_{BB}^{tot} is the renormalization of bare response R_{BB} due to the coupling in r.h.s. of Eq. (3)) is unstable then its gain rate gets added to κ_σ in the determination of $\langle |B|^2 \rangle$ since in all theories which allow factorization of 4-point correlation function into product of 2-point correlation functions, $\langle B(1)B^*(2) \rangle = R_{BB}^{\text{tot}}(1, 1')S(1', 2')R_{BB}^{\text{tot}*}(2', 2)$. Here, $S(1, 2) \equiv \langle \sigma^*(1)\sigma(2) \rangle \langle E(1)E^*(2) \rangle \simeq \langle \sigma^*(1) \rangle \langle \sigma(2) \rangle \langle E(1)E^*(2) \rangle$ and “1,” “2,” etc., mean a set of all spatial and temporal arguments.

IV. CONVECTIVE INSTABILITY VERSUS ABSOLUTE INSTABILITY

In this section, we show that the dispersion relations, Eqs. (17) and (37), predict absolute instability for large intensities. We first consider the dispersion relation, Eq. (17), which has branch cut in the complex $\tilde{\kappa}$ -plane connecting two branch points $\tilde{\kappa}_1 = 1 - \tilde{\omega} \frac{c_s}{c} - 2i \frac{c_s}{c} \frac{1}{T_c}$ and $\tilde{\kappa}_2 = -\tilde{\omega} \frac{c_s}{c} - 2i \frac{c_s}{c} \frac{1}{T_c}$.

Absolute instability occurs if the contour $Im(\tilde{\omega}) = \text{const}$ in the complex ω -plane cannot be moved down to the real $\tilde{\omega}$ axis because of pinching of two solutions of Eq. (17) in the complex $\tilde{\kappa}$ -plane.^{19,20} To describe instability one of these solutions must cross the real axis in $\tilde{\kappa}$ -plane as the contour $Im(\tilde{\omega}) = \text{const}$ is moving down. The pinch occurs provided

$$\frac{\partial \Delta_\sigma(\tilde{\omega}, \tilde{\kappa})}{\partial \tilde{\kappa}} = 0. \quad (41)$$

The pinch condition (41) together with the requirement of crossing the real axis in $\tilde{\kappa}$ -plane result in

$$\tilde{\kappa} = \frac{1}{2} + \frac{1}{2}i\sqrt{\mu\tilde{I} - 1} - \frac{c_s}{c}\tilde{\omega} - \frac{c_s}{c}\frac{2i}{T_c}. \quad (42)$$

Taking Eq. (42) together with $\Delta_\sigma(\tilde{\omega}, \tilde{\kappa}) = 0$ from Eq. (17) at the absolute instability threshold $Im(\tilde{\omega}) = 0$, gives the transcendental expression

$$\begin{aligned} \mu - \frac{1}{2}(\mu\tilde{I}_{\text{absthrsh}} - 1)^{1/2} + \frac{c_s}{c}\frac{2}{T_c} \\ - \frac{1}{2}\mu\tilde{I}_{\text{absthrsh}}\arctan\left[(\mu\tilde{I}_{\text{absthrsh}} - 1)^{-1/2}\right] = 0 \end{aligned} \quad (43)$$

for the absolute instability threshold intensity $\tilde{I}_{\text{absthrsh}}$. Assuming $\mu\tilde{I}_{\text{absthrsh}} \gg 1$ we obtain from Eq. (43) an explicit expression for the CBSBS absolute instability threshold

$$\tilde{I}_{\text{absthrsh}} = \mu + 3\mu^{-1} + O(\mu^{-3}) + O(\tilde{T}_c^{-1}c_s/c). \quad (44)$$

The absolute instability threshold for the second RPA-like branch, Eq. (37), is obtained similarly with the pinch condition $\frac{\partial \Delta_B(\tilde{\omega}, \tilde{\kappa})}{\partial \tilde{\kappa}} = 0$. It gives the absolute instability threshold for the RPA-like branch of instability

$$\tilde{I}_{\text{absthrsh}, B} = \mu \left(1 + \frac{1}{\mu\tilde{T}_c}\right)^2. \quad (45)$$

For $\tilde{T}_c \lesssim 1$, the threshold given by Eq. (44) is lower than that given by Eq. (45) and thus Eq. (45) can be ignored.

For $\mu \gg 1$ the absolute threshold given by Eq. (44) reduces to the coherent absolute BSBS instability threshold

$$\tilde{I}_{\text{absthrshcoherent}} = \mu. \quad (46)$$

For typical experimental condition $\mu \gtrsim 5$ as discussed in Sec. VI. Then the absolute instability threshold found in Eq. (44) is significantly above the convective instability threshold given by (24). Thus in simulations described below we emphasize the convective regime and assume \tilde{I} to be below the absolute threshold.

V. NUMERICAL SIMULATIONS

We performed two types of simulations. The first type is 3 + 1D simulations (three spatial coordinates \mathbf{r} , z , and t) of Eqs. (3), (4), and (7) with boundary and initial conditions given by Eqs. (5) and (6) in the limit $c/c_s \rightarrow \infty$ (i.e., setting $c^{-1} = 0$ in Eqs. (3) and (4)). It implies that the phases $\phi_{\mathbf{k}_j}(t - z/c)$ in Eq. (7) become only t -dependent, $\phi_{\mathbf{k}_j}(t)$. That formal limit $c \rightarrow \infty$, is consistent provided $cT_c \gg L_{\text{speckle}}$. Then in the linear instability regime, the laser field, E , at any time may be obtained by propagation from $z = 0$ while the scattered light field, B is obtained by backward propagation from $z = L_z$. Time scales are now set by the minimum of T_c and the acoustic time scale for the density σ^* . We performed numerical simulation of B and σ^* via a split-step (operator splitting) method. E advances only due to diffraction and is determined exactly by (7). For given σ^* , B is first advanced due to diffraction in transverse Fourier space, and then the source term (r.h.s. of (3) which is $\propto \sigma^*E$) is added for all $\mathbf{r} = (x, y)$. The density σ^* is evolved in the strong damping approximation in which the d/dz term is omitted from Eq. (4). In the regimes of interest, in particular, near the collective threshold, Eq. (24), regime, even for ν_{id} 's physically smallest value of 0.01, the scaled damping μ is approximately 5 while $d/d\tilde{z}$ is either $\simeq \tilde{\kappa}_i$ or $1/10$ (an inverse speckle length in scaled units). We again use tilde where necessary to stress that we performed simulations in dimensionless units. So given E and B , σ^* may be advanced in time at each z , for each transverse Fourier mode, or since the transverse Laplacian term is estimated as unity in magnitude (based on the speckle width estimate of $F\lambda_0$), σ^* may be approximately advanced at each spatial lattice point.

The second type is 2 + 1D simulations (two spatial coordinates x , z , and t) of Eqs. (3), (4), and (7) with finite value $c_s/c = 1/500$ (a typical value for actual LPI experiments) and modified top-hat boundary condition

$$|E_{\mathbf{k}}| = k^{1/2} \text{const}, \quad k < k_m; \quad E_{\mathbf{k}} = 0, \quad k > k_m, \quad (47)$$

chosen to mimic the extra factor k in the integral over transverse direction of the full 3 + 1D problem. That modified top hat choice ensures that the linearized equations of that 2 + 1D problem gives exactly the same analytical solutions, Eqs. (17) and (37), as for the full 3 + 1D problem. We used again the split-step method by integrating along the characteristics of σ and B and solving for the diffraction by Fourier transform in the transverse coordinate x .

We run simulations in the box $0 < \tilde{z} < \tilde{L}_z$. For both types of simulations, the boundary conditions for B were set at $\tilde{z} = \tilde{L}_z$. The boundary condition for the Fourier modes $\hat{B}(\mathbf{k}, z = L_z, t)$ is random time-independent phases, chosen statically independent for each \mathbf{k} . The boundary condition for σ is zero value. As time progresses, both $|\sigma|$ and $|B|^2$ grow until reaching a statistical steady state if the value of \tilde{I} is below the threshold of absolute instability, Eq. (44). Figure 6 shows a typical time dependence of $\langle |B|^2 \rangle_x$, where $\langle \dots \rangle_x$ means averaging over the transverse coordinate x . Because Eqs. (3) and (4) are linear, the maximum value of $\langle |B|^2 \rangle_x$ grows with increase \tilde{L}_z and the boundary condition $\hat{B}(\mathbf{k}, z = L_z, t)$ is defined up to multiplication by an arbitrary constant. The z -dependence of $\langle |B|^2 \rangle_x$ in the statistical steady state appears very close to exponential, $\langle |B|^2 \rangle_x \propto e^{-2\tilde{\kappa}_i \tilde{z}}$ well inside the interval $0 < \tilde{z} < \tilde{L}_z$. Near the boundaries $\tilde{z} = 0$ and $\tilde{z} = \tilde{L}_z$ there are short transition layers. The particular form of the boundary conditions for B and σ affect only these transition layers while $\tilde{\kappa}_i$ is insensitive to them.

To recover $\tilde{\kappa}_i$ with high precision, we performed simulations for a long time interval after reaching statistical steady state and averaged $\langle |B|^2 \rangle_x$ over that time at each \tilde{z} (i.e., we assumed ergodicity). We checked from simulations that equivalently one can instead use $\langle |\sigma|^2 \rangle_x$ to recover $\tilde{\kappa}_i$ which gave the same value of $\tilde{\kappa}_i$ as expected. For example, $\tilde{T}_c = 0.1$ (the time the laser light travels $\simeq 5$ laser speckles) we use 256 transverse Fourier modes (convergence of results with the number of transverse modes and the simulation box size in x were also checked) and discrete steps $\Delta\tilde{z} = 0.15$ in dimensionless units with the typical length of the system $\tilde{L}_z = 50$ ($\simeq 5$ speckle lengths) and a time step $\Delta\tilde{t} = \Delta\tilde{z}c_s/c$. For this particular set of parameters it implies $\Delta\tilde{t} = 1.5 \times 10^{-4}$. For smaller \tilde{T}_c and, respectively, smaller $\tilde{\kappa}_i$, we increased \tilde{L}_z to maintain high precision in recovering $\tilde{\kappa}_i$. Simulations typically required $\sim 10^5$ – 10^6 time steps to achieve a robust statistical steady state and then time averages were evaluated over another $\sim 10^5$ – 10^6 time steps (together with averaging over the transverse coordinate) to find $\tilde{\kappa}_i$ with high precision. After that the logarithmic derivative of $|B|^2$ (which was averaged over the transverse coordinate in addition to averaging over time) was calculated. This resulting logarithmic derivative as a function of \tilde{z} was smoothed using the moving-average (also known as sliding-window or window-average) algorithm. In order to avoid influence of transition layers on both ends of \tilde{L}_z we discarded intervals at boundaries. For example, in the case of $\tilde{L}_z = 50$ we used the interval from $\tilde{z} = 10$ to $\tilde{z} = 40$ in order to determine $\tilde{\kappa}_i$. Values of the smoothed logarithmic derivative in this interval are analyzed as follows: we take largest and

lowest values and their arithmetic mean in our estimated value of the spatial gain rate while we use the absolute value of half the difference of the largest and lowest values as a conservative error estimate. Such an approach is similar to using the L_∞ norm which yields the most conservative of error estimation. We illustrate this technique in Figure 5.

As mentioned before, we wait till the statistically steady state is approaching and after that the time averaging of $\langle |B|^2 \rangle_x$ commenced. Typical $|B|^2$ dynamics is illustrated in Figure 6. The error in evaluation of $\tilde{\kappa}_i$ decreases with increase of the averaging time \tilde{t}_{av} as seen in Figure 7. Noted that strong fluctuation can affect the process of calculation of logarithmic derivative significantly, increasing the averaging time required to achieve reasonable accuracy.

For practical purposes, it is interesting to estimate the time t_{ini} at which the initial thermal fluctuations of $|B|^2$ are amplified by $\sim e^{20}$ to reach the comparable intensity with the laser pump. We obtained from simulations that $\tilde{t}_{ini} \sim 0.7$ for $\tilde{L}_z \simeq$ two laser speckles (relevant for gold plasma in ICF experiments and corresponds to $\tilde{L}_z \simeq 22$ in dimensionless units), $\tilde{I} = 3$ and $\tilde{T}_c = 0.1$. In dimensional units for NIF conditions $t_{ini} \sim 20$ ps which is well below hydrodynamic time (several hundreds of ps).

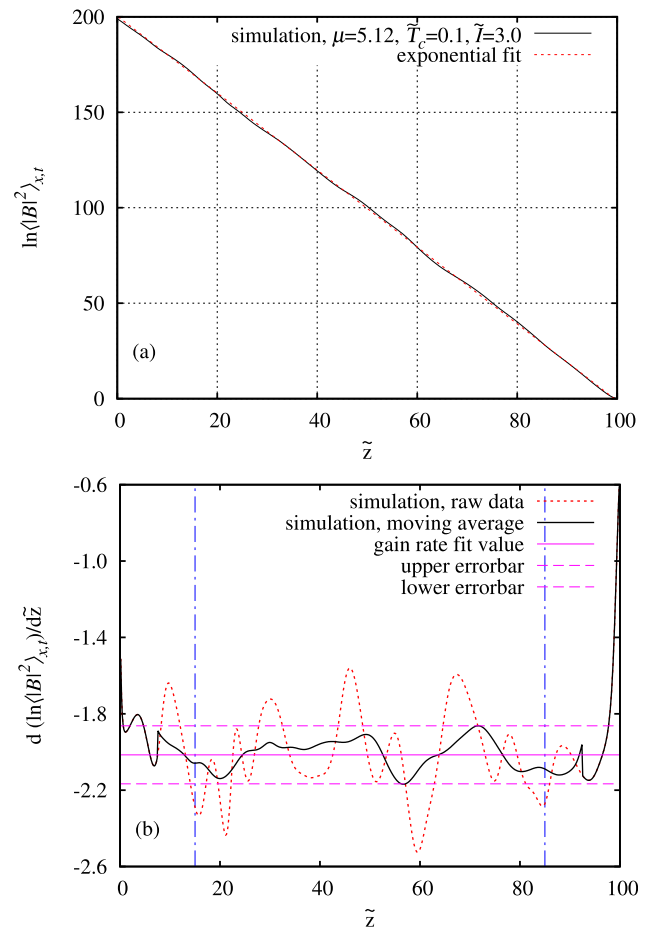


FIG. 5. Illustration of technique of spatial gain rate, κ_i , evaluation from simulations. (a) The averaged intensity $\langle |B|^2 \rangle_x$ with superimposed exponential function corresponding to the spatial gain rate. (b) The logarithmic derivative with window of used values of \tilde{z} (show by vertical lines) and largest and lowest values of spatial gain rate (horizontal lines).

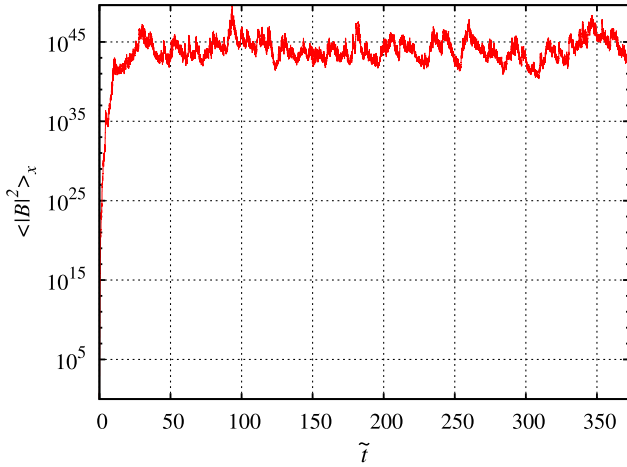


FIG. 6. The time dependence of $\langle |B|^2 \rangle_x$ for 2+1D simulation with $\tilde{L}_z = 50$, $\mu = 5.12$, $\tilde{T}_c = 0.1$, and $\tilde{I} = 3.0$. $\langle |B|^2 \rangle_x$ is shown at $\tilde{z} = 25$. It is seen that after the initial growth, $\langle |B|^2 \rangle_x$ settles into an apparent statistical steady state with the large fluctuations around it. The boundary condition at $\tilde{z} = \tilde{L}_z$ is $\langle |B|^2 \rangle_x \sim 1$.

Figure 2 shows normalized autocorrelation functions $\langle E(\tilde{\mathbf{r}}, \tilde{z}, \tilde{t})E^*(\tilde{\mathbf{r}}, \tilde{z}, \tilde{t} + \Delta\tilde{t}) \rangle$, $\langle B(\tilde{\mathbf{r}}, z, t)B^*(\tilde{\mathbf{r}}, \tilde{z}, \tilde{t} + \Delta\tilde{t}) \rangle$, and $\langle \sigma(\tilde{\mathbf{r}}, \tilde{z}, \tilde{t})\sigma^*(\tilde{\mathbf{r}}, \tilde{z}, \tilde{t} + \Delta\tilde{t}) \rangle$ for $\tilde{T}_c = 0.1$ determined from simulations (we averaged here over time for each fixed values of $\tilde{\mathbf{r}}$, \tilde{z} , and \tilde{L}_z). It is seen that the correlation times for E and B are similar while the correlation time for σ is much larger, the more so the smaller \tilde{T}_c . This justifies the analytical

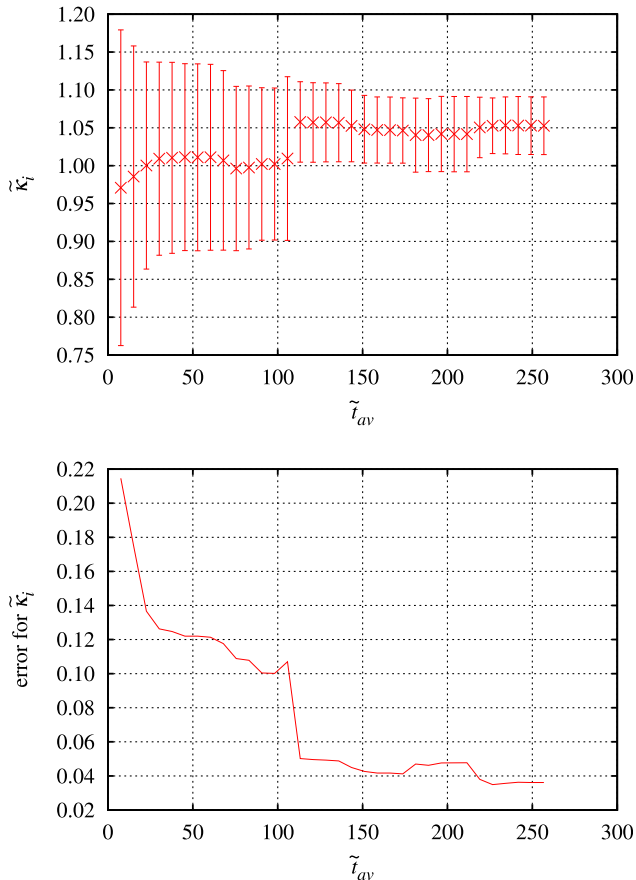


FIG. 7. Dependence of the spatial gain rate on averaging time \tilde{t}_{av} . Upper panel: the spatial gain rate with error bars. Lower panel: relative error for the spatial gain rate.

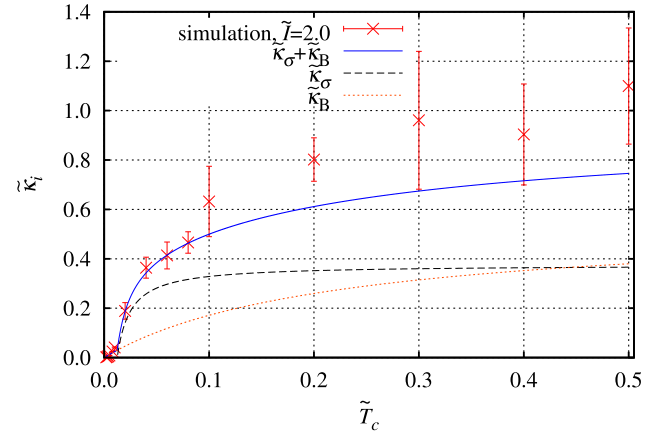


FIG. 8. BSBS spatial gain rates vs. \tilde{T}_c as in Figure 3 but with $\tilde{I} = 2$ and $\mu = 5.12$.

approximations used in Sec. III. We also varied $\tilde{\mathbf{r}}$, \tilde{z} , and \tilde{L}_z and obtained the same results for the correlation times within statistical error.

Figures 1, 3, and 8–10 show the spatial gain rates extracted from multiple simulations. Figures 8–10 are similar to Figure 3 but show values of $\tilde{\kappa}_B + \tilde{\kappa}_{\sigma}$, $\tilde{\kappa}_B$, and $\tilde{\kappa}_{\sigma}$ compared with the spatial gain rate $\tilde{\kappa}_i$ for $\tilde{I} = 2, 3$ and $\mu = 5.12, 51.2$.

VI. APPLICABILITY OF THE DISPERSION RELATION

To find applicability conditions of the Bouret approximation used in derivation of Eqs. (17) and (37), we determine the effective bandwidths $\Delta\omega_B$ and $\Delta\omega_{\sigma}$ for B and σ , respectively. Following Ref. 9, we estimate these bandwidths through the frequency mismatches in three-wave interactions for equations (2), (3), and (4).

There are two sources of mismatches in these equations: the temporal incoherence (5) of the pump wave E with temporal bandwidth $\Delta\omega_0 \equiv 1/T_c$ and the spatial incoherence of E in the top hat model (6).

The temporal bandwidth $\Delta\omega_0$ results in the spectral width $\Delta k_0 \equiv \Delta\omega_0/c$. Counter-propagation of E and B results in the effective contribution $2c\Delta k_0 = 2/T_c$ to the temporal bandwidth of B . Co-propagation of E and σ with the relative

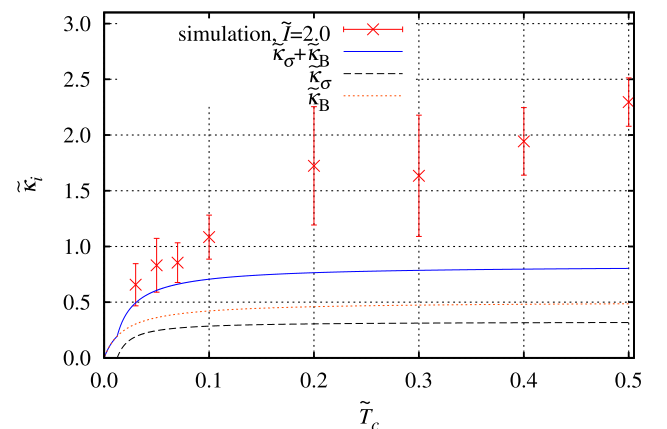


FIG. 9. BSBS spatial gain rates vs. \tilde{T}_c as in Figure 3 but with $\tilde{I} = 2$ and $\mu = 51.2$.

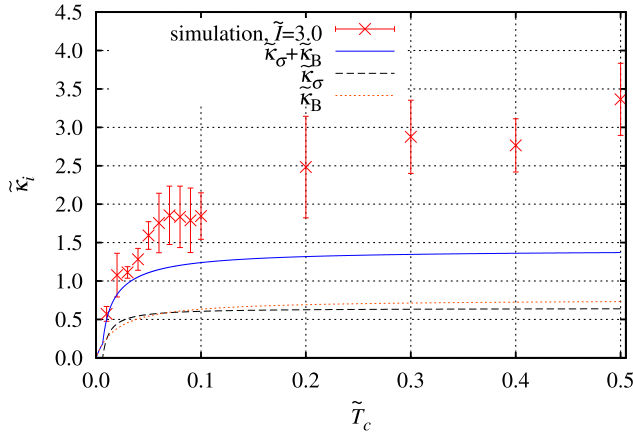


FIG. 10. BSBS spatial gain rates vs. \tilde{T}_c as in Figure 3 but with $\tilde{I} = 3$ and $\mu = 51.2$.

velocity $c - c_s$ results in the effective contribution $(c - c_s)\Delta k_0 \simeq c\Delta k_0 = 1/T_c$ to the temporal bandwidth of σ .

The top-hat distribution in Fourier space has the transverse width $k_m = k_0/2F$. That transverse width results in the effective contribution $ck_m^2/(2k_0) = k_0c/(8F^2)$ to the temporal bandwidth of B . Its contribution to the temporal bandwidth of $\sigma \sim c_s k_m^2/(2k_0)$ is neglected below because $c_s/c \ll 1$.

We use again tilde to express all quantities in the dimensionless units (as described after Eq. (8)) thus obtaining

$$\begin{aligned}\Delta\tilde{\omega}_B &= \frac{2}{\tilde{T}_c} + \frac{1}{2c_s}, \\ \Delta\tilde{\omega}_\sigma &= \frac{1}{\tilde{T}_c},\end{aligned}\quad (48)$$

where in the first equation we added contributions from both temporal and spatial incoherence.

To find the range of applicability of the Bourret approximation, we have to compare (48) with the typical values of propagators (inverse of the bare response functions) cR_{BB}^{-1} and $c_sR_{\sigma\sigma}^{-1}$ acting on the perturbations $\langle B \rangle, \langle \sigma^* \rangle \propto e^{i(kz + \mathbf{k}\cdot\mathbf{r} - \omega t)}$. We estimate these values as follows:

$$\begin{aligned}|D_B| &\equiv \frac{k_0c_s}{4F^2} |\tilde{D}_B| \equiv \left| \frac{cR_{BB}^{-1}\langle B \rangle}{\langle B \rangle} \right| \\ &\simeq \left| \omega + \kappa c - \frac{k_m^2}{2k_0} c \right| \simeq \frac{k_0c_s}{4F^2} \frac{c}{c_s} |\tilde{\kappa} - 1/2|\end{aligned}\quad (49)$$

and

$$\begin{aligned}|D_\sigma| &\equiv \frac{k_0c_s}{4F^2} |\tilde{D}_\sigma| \equiv \left| \frac{cR_{\sigma\sigma}^{-1}\langle \sigma \rangle}{\langle \sigma \rangle} \right| \\ &\simeq |\omega - \kappa c_s + 2i\nu_{ia}k_0c_s| = \frac{k_0c_s}{4F^2} |\tilde{\omega} - \tilde{\kappa} + i\mu|.\end{aligned}\quad (50)$$

The applicability of the Bourret approximation for $\langle B \rangle$ and $\langle \sigma \rangle$ requires that⁹

$$\begin{aligned}\Delta\tilde{\omega}_B &> |\tilde{D}_B|, \\ \Delta\tilde{\omega}_\sigma &> |\tilde{D}_\sigma|,\end{aligned}\quad (51)$$

as well as

$$\Delta\tilde{\omega}_B\Delta\tilde{\omega}_\sigma > \tilde{\gamma}_0^2, \quad (52)$$

where $\tilde{\gamma}_0$ is the temporal growth rate of the spatially homogeneous solution given by $\tilde{\gamma}_0^2 = (1/4)(c/c_s)\mu\tilde{I}$.

Combining Eqs. (48)–(51), we obtain (assuming $\frac{1}{4\tilde{T}_c} \frac{c}{c_s} \gg 1$) the conditions

$$|\tilde{\kappa} - 1/2| < 1/2 \quad (53)$$

and

$$\tilde{T}_c < 1/|\tilde{\omega} - \tilde{\kappa} + i\mu|. \quad (54)$$

Condition Eq. (53) shows that as $\tilde{\kappa}_i$ increases up to values ~ 1 with the increase of \tilde{T}_c , the validity of Eqs. (17) and (37) breaks down. It suggests an explanation why for $\tilde{\kappa}_i \geq 1$ we see deviation of $\tilde{\kappa}_B + \tilde{\kappa}_\sigma$ from $\tilde{\kappa}_i$ as in Figure 1(b) for $\tilde{I} = 3$. Condition Eq. (52) results in $\tilde{T}_c < 2/(\mu\tilde{I})$. At the convective threshold Eq. (27), it reduces to $\tilde{T}_c < \pi/(2\mu)$. This inequality is however a little less restrictive than condition Eq. (54).

Condition Eq. (54) simplifies for $|\tilde{\kappa} - \tilde{\omega}| \leq 1$ to

$$\tilde{T}_c < 1/\mu, \quad (55)$$

because typically $\mu \gg 1$ as discussed below in this section.

Approximating $\tilde{\kappa}_i$ as $\tilde{\kappa}_B + \tilde{\kappa}_\sigma$ also requires that both $\tilde{\kappa}_B$ and $\tilde{\kappa}_\sigma$ are unstable which implies that $\tilde{I} > \tilde{I}_{convthresh}$. Otherwise, if $\tilde{I} < \tilde{I}_{convthresh}$ then $\tilde{\kappa}_\sigma \sim \mu$ as given by the stable branch solution Eq. (29) which contradicts Eq. (53) for typical $\mu \gg 1$.

We then distinguish the following cases:

- If $\tilde{I} < 4/\pi$ then $\tilde{I} < \tilde{I}_{convthresh}$ for any \tilde{T}_c as follows from Eqs. (24) and (27). In that case there is no range of applicability of $\tilde{\kappa}_B + \tilde{\kappa}_\sigma$ as the approximation of $\tilde{\kappa}_i$. This is consistent with $\tilde{\kappa}_i$ from simulations for $\tilde{I} = 1$ shown by squares in Figure 1. These squares do not agree with dashed lines which shows $\tilde{\kappa}_B + \tilde{\kappa}_\sigma$ (in this case $\tilde{\kappa}_B + \tilde{\kappa}_\sigma$ is replaced by $\tilde{\kappa}_B$ because $\tilde{\kappa}_\sigma$ is stable according to $\tilde{I} < \tilde{I}_{convthresh}$).
- If $\tilde{I} > 4/\pi$ then $\tilde{I} > \tilde{I}_{convthresh}$ for

$$\tilde{T}_c > \frac{4c_s}{c} \tan(2/\tilde{I}), \quad (56)$$

as follows from Eq. (24). In that case $\tilde{\kappa}_B + \tilde{\kappa}_\sigma$ can approximate $\tilde{\kappa}_i$ provided (57) is also satisfied. This is consistent with cases for $\tilde{I} = 2, 3$ shown in Figures 1, 3, and 8–10.

We note that Eq. (54) together with Eq. (56) results in a double inequality

$$\tan(2/\tilde{I}) < \tilde{T}_c < 1/\mu, \quad (57)$$

which can be well satisfied for $\mu \simeq 5$, i.e., $\nu_{ia} \simeq 0.01$ as in gold ICF plasma (for typically values $c_s/c \simeq 1/500$ and $F = 8$). But for ICF plasma with a low ionization number Z which typically has $\nu_{ia} \simeq 0.1$, we obtain that $\mu \simeq 50$ making (57) valid only in a narrow range of values of \tilde{T}_c . This is consistent with Figures 9 and 10 where $\tilde{\kappa}_B + \tilde{\kappa}_\sigma$ agrees with $\tilde{\kappa}_i$ in much narrower range of \tilde{T}_c values than in Figures 3 and 8.

We now consider the applicability of RPA for intensity $\langle |B|^2 \rangle$ (or equivalently for $\langle |\sigma|^2 \rangle$). In addition to conditions (51) and (52), RPA requires also the inequality complementary to (51) as follows:⁹

$$\begin{aligned} \Delta\tilde{\omega}_B &> |\tilde{D}_\sigma|, \\ \Delta\tilde{\omega}_\sigma &> |\tilde{D}_B|. \end{aligned} \quad (58)$$

Combining Eqs. (48)–(50), we obtain that the first condition in Eq. (58) is trivially satisfied while the second one results in a very strict condition

$$\tilde{T}_c < \frac{c_s}{c} \frac{1}{|\tilde{\kappa} - 1/2|}. \quad (59)$$

For very small \tilde{T}_c satisfying condition Eq. (59), the RPA spatial gain rate for the intensity $\langle |B|^2 \rangle$ coincides with Eq. (39) and thus Eq. (59) reduces to

$$\tilde{T}_c < \frac{2c_s}{c} \simeq \frac{1}{250}. \quad (60)$$

In non-scaled units the condition (60) is given by

$$cT_c < (4/7\pi)L_{\text{speckle}}. \quad (61)$$

Figure 3(c) shows that indeed under condition Eq. (60), the RPA spatial gain rate Eq. (39) is in excellent agreement with simulations. However, the range of T_c satisfying condition Eq. (60) is not practical for ICF applications. The very stringent condition Eq. (60) explains why we have to approximate κ_i by the sum of the spatial gain rates $\kappa_B + \kappa_\sigma$ for amplitudes but not to use the RPA spatial gain rate for intensity.

We now discuss a broader picture. Depending on laser incoherence we have a hierarchy of thresholds

- (a) Spatially incoherent laser beam with large $\tilde{T}_c \gg 1$ has threshold,

$$\tilde{I}_{\text{thresholdspeckle}} = 4/7\pi, \quad (62)$$

beyond which reflectivity is dominated by intense speckles (independent hot spot model) as found in Refs. 5, 12, 21, and 22.

- (b) The convective instability spatial gain rate for spatially and temporarily incoherent beam with T_c satisfying Eq. (57) is given by $\kappa_B + \kappa_\sigma$. The convective threshold Eq. (27) for κ_σ is a factor 7 times higher compared with the speckle threshold Eq. (62). It indicates a practical limit of how the BSBS instability threshold can be increased by decreasing T_c until it falls into the range given by Eq. (57). For example, as seen in Figure 1(b), if we take the typical value $\tilde{T}_c = 1$ inside that range, and decrease the laser intensity 3 fold from $\tilde{I} = 3$ to $\tilde{I} = 1$ to fall below CBSBS threshold, then the spatial gain rate decreases by a factor 5. Further decrease of \tilde{I} below 1 would result in slower (near-linear) decrease of the spatial gain rate. Similarly, if we decrease \tilde{T}_c below $\tilde{T}_c = 1$ for fixed \tilde{I} then the decrease of the spatial gain rate will be quick for $\tilde{I} = 3$ (above CBSBS

threshold) and slow for $\tilde{I} = 1$ (below CBSBS threshold).

- (c) For much smaller T_c satisfying the condition (61), the classical RPA regime is recovered which has ignorable diffraction (Refs. 7, 9, and 23) and the spatial gain rate $\tilde{\kappa}_i \simeq \mu\tilde{I}/\tilde{T}_c$ as in Eq. (39). This limit (e.g., for $\lambda_0 = 351$ nm and $F = 8$ it requires $T_c < 0.1$ ps) which is not relevant for ICF as T_c is too small.

VII. ESTIMATES FOR EXPERIMENT

For nominal NIF parameters,^{1,11} $F = 8$, $n_e/n_c = 0.1$, $\lambda_0 = 351$ nm, $c_s = 6 \times 10^7$ cm s⁻¹, and electron plasma temperature $T_e \simeq 2.6$ keV (T_e was recently updated from the old standard value $T_e \simeq 5$ keV (Ref. 24)), we obtain from Eq. (27) that $I_{\text{convthresh}} \simeq 1.1 \times 10^{14}$ W/cm² for gold plasma with $\nu_{ia} \simeq 0.01$ which is in the range of NIF single polarization intensities. Fig. 11 shows κ_i in the limit $c_s/c = 0$, $\tilde{T}_c \rightarrow 0$ from simulations, analytical result $\tilde{\kappa}_\sigma$ ($\kappa_B = 0$ in that limit) and the instability spatial gain rate of the coherent laser beam $\kappa_{\text{coherent}} = \mu/2 - (\mu^2 - \mu\tilde{I})^{1/2}/2$ (see, e.g., Ref. 4). It is seen that the coherent κ_i significantly overestimates simulation based κ_i especially around $I_{\text{convthresh}}$ Eq. (27). The convective gain rate κ_i has a significant dependence on \tilde{T}_c if we include the effect of finite $c/c_s = 500$ and finite \tilde{T}_c as in Fig. 1(b). Current NIF 3 Å beam smoothing design has $T_c \simeq 4$ ps implying $\tilde{T}_c \simeq 0.15$. In that case Fig. 1(b) shows that there is a significant (about 5 fold) change in κ_i between $\tilde{I} = 1$ and $\tilde{I} = 3$. Similar estimate for KrF lasers ($\lambda_0 = 248$ nm, $F = 8$, $T_c = 0.7$ ps) gives $\tilde{T}_c = 0.04$ which results in a significant (40%) reduction of κ_i for $\tilde{I} = 3$ compared with above NIF

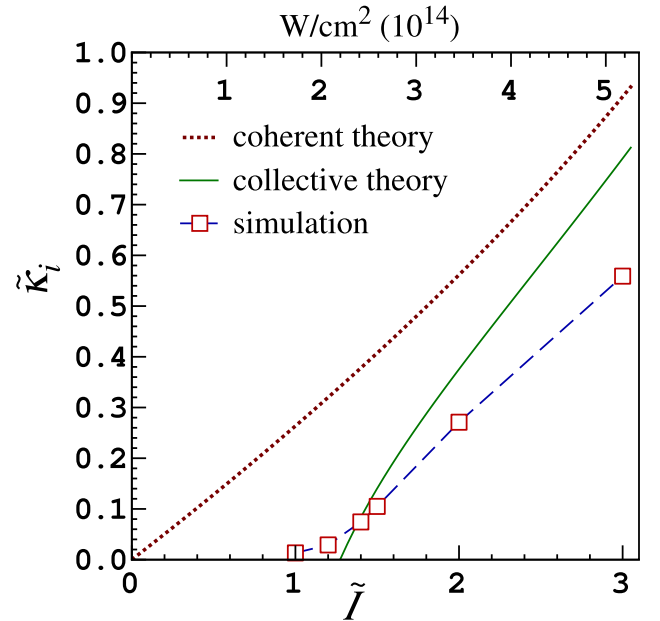


FIG. 11. $\tilde{\kappa}_i$ vs. \tilde{I} for $\mu = 5.12$ obtained from 3+1D simulations (squares connected by dashed line, $c_s/c = 0$, and limit $\tilde{T}_c \rightarrow 0$ taken by extrapolation from $\tilde{T}_c \ll 1$), analytical result $\tilde{\kappa}_\sigma$ (solid curve) and coherent laser beam spatial gain rate κ_{coherent} (dotted curve). The scaled dimensionless laser intensity \tilde{I} and damping rate μ in units of acoustic propagation time along a speckle are defined in (8). Upper grid corresponds to laser intensity in dimensional units $I_{\text{physical}} \propto T_e/\lambda_0^2$ for NIF parameters and gold plasma $T_e \simeq 5$ keV, $F = 8$, $n_e/n_c = 0.1$, $\nu_{ia} = 0.01$, $\lambda_0 = 351$ nm.

estimate. This reduction is at fixed \tilde{I} , and does not include the further reduction at fixed physical laser intensity, $I_{physical}$, due to the well known dependence on laser wavelength, $\tilde{I} \propto I_{physical} \lambda_0^2$.

The BSBS spatial gain rate κ_i may be further reduced by self-induced temporal incoherence (see, e.g., Ref. 25). Another possibility for self-induced temporal incoherence is through collective forward stimulated Brillouin scatter (CFSBS) instability which in its linear regime includes collective FSBS (CFSBS).^{10,11} For low Z plasma, the CBSBS and CFSBS thresholds are close while the latter may be lowered by adding higher Z dopant.

VIII. CONCLUSION

In conclusion, we identified the collective threshold Eq. (24) of stimulated Brillouin backscatter instability of partially incoherent laser beam for ICF relevant plasma. Above that threshold the stimulated Brillouin backscatter spatial gain rate κ_i is well approximated by the sum of the collective-like spatial gain rate κ_σ and Random Phase Approximation-like spatial gain rate κ_B . That result is in agreement with the direct stochastic simulations of stimulated Brillouin backscatter equations. Values of κ_σ and κ_B are comparable above threshold while in a small neighborhood of threshold the value of κ_i changes quickly due to either correlation time or laser intensity variation which results in passage through the collective threshold. With further increase of laser intensity, absolute instability eventually develops above the threshold, Eq. (44). Well below the threshold, the standard Random Phase Approximation result with linear dependence of κ_i on T_c is recovered.

ACKNOWLEDGMENTS

We acknowledge helpful discussions with R. Berger and N. Meezan. P.L. and H.R. were supported by the New Mexico Consortium and Department of Energy Award No. DE-SC0002238 as well as by the National Science Foundation under Grant Nos. PHY 1004118, and PHY 1004110. P.L. was partially supported by the National Science Foundation under Grant No. DMS 1412140. A.K. was partially supported by the “Leading Scientific Schools of Russia” Grant No. NSh-3753.2014.2.

¹J. D. Lindl, P. Amendt, R. L. Berger, S. G. Glendinning, S. H. Glenzer, S. W. Haan, R. L. Kauffman, O. L. Landen, and L. J. Suter, *Phys. Plasmas* **11**, 339 (2004).

²N. B. Meezan, L. J. Atherton, D. A. Callahan, E. L. Dewald, S. Dixit, E. G. Dzenitis, M. J. Edwards, C. A. Haynam, D. E. Hinkel, O. S. Jones, O.

Landen, R. A. London, P. A. Michel, J. D. Moody, J. L. Milovich, M. B. Schneider, C. A. Thomas, R. P. J. Town, A. L. Warrick, S. V. Weber, K. Widmann, S. H. Glenzer, L. J. Suter, B. J. MacGowan, J. L. Kline, G. A. Kyrala, and A. Nikroo, *Phys. Plasmas* **17**, 056304 (2010).

³D. H. Froula, L. Divol, N. B. Meezan, S. Dixit, J. D. Moody, P. Neumayer, B. B. Pollock, J. S. Ross, and S. H. Glenzer, *Phys. Rev. Lett.* **98**, 085001 (2007); X. Meng, C. Wang, H. An, G. Jia, H. Zhou, and S. Fu, *High Power Laser Sci. Eng.* **1**, 94 (2013).

⁴W. L. Kruer, *The Physics of Laser Plasma Interactions* (Addison-Wesley, New York, 1990).

⁵H. A. Rose, *Phys. Plasmas* **2**, 2216 (1995).

⁶J. Garnier, *Phys. Plasmas* **6**, 1601 (1999).

⁷A. A. Vedenov and L. I. Rudakov, *Sov. Phys. Doklady* **9**, 1073 (1965); A. M. Rubenchik, *Radiophys. Quantum Electron.* **17**, 1249 (1976); V. E. Zakharov, S. L. Musher, and A. M. Rubenchik, *Phys. Rep.* **129**, 285 (1985).

⁸G. Laval, R. Pellat, D. Pesme, and A. Ramani, *Phys. Fluids* **20**, 2049 (1977).

⁹D. Pesme, R. L. Berger, E. A. Williams, A. Bourdier, and A. Bortuzzo-Lesne, *Natl. Tech. Inform. Document No. PB92-100312* (1987); e-print [arXiv:0710.2195](https://arxiv.org/abs/0710.2195) (2007).

¹⁰P. M. Lushnikov and H. A. Rose, *Phys. Rev. Lett.* **92**, 255003 (2004).

¹¹P. M. Lushnikov and H. A. Rose, *Plasma Phys. Controlled Fusion* **48**, 1501 (2006).

¹²H. A. Rose and D. F. DuBois, *Phys. Rev. Lett.* **72**, 2883 (1994).

¹³A. J. Schmitt and B. B. Afeyan, *Phys. Plasmas* **5**, 503 (1998).

¹⁴C. Niemann, R. L. Berger, L. Divol, D. H. Froula, O. Jones, R. K. Kirkwood, N. Meezan, J. D. Moody, J. Ross, C. Sorce, L. J. Suter, and S. H. Glenzer, *Phys. Rev. Lett.* **100**, 045002 (2008).

¹⁵P. M. Lushnikov and H. A. Rose, e-print [arXiv:0710.0634](https://arxiv.org/abs/0710.0634) (2007).

¹⁶The literature is replete with multi-dimensional simulations of SBS, with models which are similar to the one used in our work (see, e.g., Refs. 13, 26, and 27). However, these emphasize nonlinear regimes with competing instabilities, such as BSBS and filamentation, while we apply our theory and simulations to the strictly linear BSBS regime.

¹⁷R. H. Lehmberg and S. P. Obenschain, *Opt. Commun.* **46**, 27 (1983).

¹⁸Subsequent analysis can be easily generalized to include polarization smoothing.¹

¹⁹A. Bers, in *Handbook of Plasma Physics*, edited by M. N. Rosenbluth and R. Z. Sagdeev (North-Holland, 1983), pp. 451–517.

²⁰L. P. Pitaevskii and E. M. Lifshitz, *Physical Kinetics: Volume 10* (Butterworth-Heinemann, Oxford, 1981).

²¹H. A. Rose and Ph. Mounaix, *Phys. Plasmas* **18**, 042109 (2011).

²²H. A. Rose and D. F. DuBois, *Phys. Fluids B* **5**, 3337 (1993).

²³D. F. DuBois, B. Bezzerides, and H. A. Rose, *Phys. Fluids B* **4**, 241 (1992).

²⁴M. D. Rosen, H. A. Scott, D. E. Hinkel, E. A. Williams, D. A. Callahan, R. P. J. Town, L. Divol, P. A. Michel, W. L. Kruer, L. J. Suter, R. A. London, J. A. Harte, and G. B. Zimmerman, *High Energy Density Phys.* **7**, 180 (2011).

²⁵P. Loiseau, O. Morice, D. Teychenneé, M. Casanova, S. Hüller, and D. Pesme, *Phys. Rev. Lett.* **97**, 205001 (2006).

²⁶D. Pesme, W. Rozmus, V. T. Tikhonchuk, A. Maximov, I. Ourdev, and C. H. Still, *Phys. Rev. Lett.* **84**, 278 (2000); A. V. Maximov, I. G. Ourdev, D. Pesme, W. Rozmus, V. T. Tikhonchuk, and C. E. Capjack, *Phys. Plasmas* **8**, 1319 (2001).

²⁷P. E. Masson-Laborde, S. Hüller, D. Pesme, M. Casanova, P. Loiseau, and C. Labaune, *J. Phys. IV* **133**, 247 (2006).